

Thermal Induced Strain Relaxation of 1D Iron Oxide for Solid Electrolyte Interphase Control and Lithium Storage Improvement

Kangning Zhao, Mingying Wen, Yifan Dong, Lei Zhang, Mengyu Yan, Wangwang Xu, Chaojiang Niu, Liang Zhou,* Qiulong Wei, Wenhao Ren, Xuanpeng Wang, and Liqiang Mai*

High energy lithium ion battery based on multi-electron redox reaction is often accompanied by inherent large volume expansions, sluggish kinetics, and unstable solid electrolyte interphase layer, leading to capacity failure. Here, thermal induced strain relaxation is proposed to realize the solid electrolyte interphase control. It is demonstrated that through thermal treatment, lattice strain is well released and defect density is well reduced, facilitating the charge transfer, improving the interparticle contacts and the contacts at the interface of electrode to withstand the huge volume expansion/contraction during cycling. In this way, the as-prepared α -Fe₂O₃ electrode at 800 °C with no protective shell shows an outstanding reversible capacity of 1200 mA h g⁻¹ at 100 mA g⁻¹ and an excellent high-rate cyclability with a capacity fading of 0.056% per cycle for 1200 cycles at 5 A g⁻¹. It is expected that such findings facilitate the applications of high capacity anode and cathode material systems that undergo large volume expansion.

impeded by the poor cycling stability.^[9,12-15] Due to the huge sums of lithium ions involved, a large volume change is induced during (de)lithiation, which results in electrode disintegration and active material pulverization, thus greatly limiting cycle life. In addition, repeated volume changes would destroy preformed solid electrolyte interphase (SEI) layer and re-expose the fresh surface of the active material to the electrolyte, leading to continuous formation of SEI layer. The frequent formation of SEI layer not only consumes the electrolyte and lithium ions, but also retards the lithium ion diffusion, leading to capacity failure.^[16-18] Several strategies have been successfully adopted to control the formation of SEI layer by constructing protective layer strategy. However, the addition of coating layer would pay the price of

decreasing the total capacity, complicating the fabrication process, and increasing additional price of raw materials. Thus, it is highly desirable to improve the intrinsic property of electrode for SEI control.

1D nanostructures have stimulated considerable interests in energy storage field due to their intriguing properties.^[19-24] In order to obtain unique 1D nanostructures, various synthetic approaches have been adopted, such as chemical vapor deposition, hydrothermal treatment, electrospinning, template-engaged redox reaction, and so on.^[25-35] Among these methods, template-engaged redox reaction, which is driven by the difference in the electrochemical potentials of two redox pairs, offers great opportunities for the fabrication of 1D nanostructures with controllable pore size and composition.^[25,36-41] Combining template-engaged redox reaction with subsequent thermal treatment, 1D nanostructure with various compositions and morphologies can be obtained. However, the rational design of complex 1D nanostructure remains a considerable challenge.

Herein, we design ladder-like α -Fe₂O₃ nanostructures which are produced through a template-engaged redox reaction followed by thermal treatment. Initially, MnOOH nanowires are used as the 1D template and FeSO₄ is used as the iron sources for the redox reaction to obtain Fe(OH)₃ hierarchical nanotube precursor. Additionally, unlike previous reports, MnOOH nanowires witness an inside-out reaction process, indicating the occurrence of template-engaged redox reaction. In this

1. Introduction

Driven by the upcoming large-scale applications in consumer electronics and electric vehicles, extensive research efforts have been dedicated to high energy batteries.^[1-5] With a theoretical capacity of 1007 mA h g⁻¹ and improved safety, hematite (α -Fe₂O₃) has been regarded as one of the most promising anode materials for next-generation high energy lithium ion batteries.^[6-11] However, its practical application is strongly

K. N. Zhao, M. Y. Wen, Y. F. Dong, L. Zhang, M. Y. Yan,
C. J. Niu, Prof. L. Zhou, Q. L. Wei, W. H. Ren,
X. P. Wang, Prof. L. Q. Mai
State Key Laboratory of Advanced Technology
for Materials Synthesis and Processing
Wuhan University of Technology
Wuhan 430070, China
E-mail: liangzhou@whut.edu.cn; mlq518@whut.edu.cn



Y. F. Dong
Department of Chemistry
University of Wisconsin–Madison
WI 53706, USA

W. W. Xu
Department of Mechanical and Industrial Engineering
Louisiana State University
70803 Baton Rouge, LA, USA

DOI: 10.1002/aenm.201601582

regard, our process is principally different. During the subsequent thermal treatment, it is found that thermal induced strain relaxation plays an important role in the morphology as well as the electrochemical performance of the products. The resultant ladder-like α -Fe₂O₃ nanostructures at 800 °C with no obvious grain boundary are able to offer the least internal strain and defect for good structural integrity, low charge transfer resistance as well as thin and stable SEI layer formation to inhibit capacity failure. In this way, the ladder-like α -Fe₂O₃ manifests excellent electrochemical performances. Specifically, it shows a very high reversible capacity (1200 mA h g⁻¹ after 50 cycles at 100 mA g⁻¹) and excellent high-rate cycling stability (capacity fading of 0.056% per cycle against the second cycle at 5 A g⁻¹). To the best of our knowledge, ladder-like α -Fe₂O₃ nanostructures we report here show the best cycling stability (up to 1200 cycles) among α -Fe₂O₃ anode materials (Table S1, Supporting Information).

2. Results and Discussion

A typical synthesis process starts from the hydrothermal synthesis of MnOOH nanowires (Figure S1b,c, Supporting Information) as the template. When FeSO₄ is added to MnOOH suspension, partial hydrolysis of Fe²⁺ ions ($[\text{Fe}(\text{H}_2\text{O})_6]^{2+} \rightarrow [\text{Fe}(\text{OH})(\text{H}_2\text{O})_5]^+ + \text{H}^+$) generates an acidic environment, facilitating the subsequent redox reaction.^[38] The standard reduction potential of Fe³⁺/Fe²⁺ pair (0.77 V vs Standard Hydrogen Electrode (SHE)) is lower than that of MnOOH/Mn²⁺ (1.65 V vs SHE) (see the Supporting Information). As a result, Fe²⁺ is oxidized to Fe³⁺ by MnOOH, while MnOOH is reduced to Mn²⁺: $\text{Fe}^{2+} + \text{MnOOH} + 3\text{H}^+ \rightarrow \text{Fe}^{3+} + \text{Mn}^{2+} + 2\text{H}_2\text{O}$.^[42–44] This reaction mainly takes place at the surface of MnOOH nanowires. A thin Fe(OH)₃ layer immediately forms on the surface of MnOOH nanowires through the following reaction: $[\text{Fe}(\text{H}_2\text{O})_6]^{3+} \rightarrow \text{Fe}(\text{OH})_3(\text{s}) + 3\text{H}^+ + 3\text{H}_2\text{O}$.^[36,38] Unlike previous reports, we carefully selected the oxidation of iron species rather than reduction. As K_{sp} of Fe(OH)₂ (4.87×10^{-17}) is much higher than Fe(OH)₃ (2.64×10^{-39}), we can rule out acid etching reaction (released by hydrolysis of Fe³⁺). This is further elucidated by time-dependent experiment to investigate structural evolution from MnOOH nanowires to Fe(OH)₃ hierarchical nanotubes. Transmission electron microscopy (TEM) is utilized to characterize the products at different reaction times from 10 min to 12 h (Figure 1b–g). After 10 min of reaction, a thin layer of Fe(OH)₃ forms on the surface of MnOOH nanowire (Figure 1b). After 30 min of reaction, hierarchical Fe(OH)₃@MnOOH core–shell structures is obtained (Figure 1c). After 1 h of reaction, small voids are observed in the center of the nanowire (Figure 1d), indicating that solid-state diffusion has to take place in order to form the hollow structure when a complete Fe(OH)₃ shell is formed. After reacting for 2 h, the voids in the MnOOH core become more obvious (Figure 1e), suggesting that the randomly distributed small voids condense into large voids during the reaction. The void in the center of the nanowires gets larger after 6 h (Figure 1f) and finally stabilizes after 12 h (Figure 1g), giving rise to the Fe(OH)₃ hierarchical nanotubes. It should be mentioned that the voids are usually first observed at the interface of sacrificial template and target material in template-engaged redox reactions,^[36,38] which

means that the template experiences an inside-out reaction process. However, in our case, voids are first developed in the center of the MnOOH nanowires rather than at the interface of Fe(OH)₃/MnOOH. This suggests that MnOOH nanowires experience an inside-out redox reaction and the solid-state diffusion of Mn²⁺ diffuses toward the interface. This phenomenon also rules out the possibility of acid etching. Because acid etching process usually involves the dissolution of core and the formation of shell while there appear voids between core and shell. This is quite different from what we observed here. Thus, due to the sluggish solid-state diffusion,^[45,46] a much longer reaction time (12 h) is required for the reaction.^[45,47] In this regard, mechanism involved for the hollow architecture in the present system is principally different from the previous reports. The Fe/Mn atomic ratio during reaction is shown in Energy-dispersive X-ray Spectroscopy (EDS) and the results are shown in Figure S3 and Table S2 (Supporting Information). The EDS results indicate that the reaction proceeds fast in the initial stage and slows down gradually with the reaction going on, which is consensus to our assumption. The MnOOH nanowire is completely consumed after 12 h (Table S2, Supporting Information). All these confirm the occurrence of redox-engaged reaction rather than driven by acid etching.

The crystallographic structure, phase purity, and morphology are examined by X-ray powder diffraction (XRD) and scanning electron microscopy (SEM), as shown in Figure S1 (Supporting Information). MnOOH template is well crystallized (Figure S1a, Supporting Information) and shows a uniform 1D nanowire morphology with a diameter of ≈ 100 nm (Figure S1b,c, Supporting Information). After the redox reaction, the diffraction peaks from MnOOH phase entirely disappears, indicating the complete consumption of MnOOH. The resulting XRD pattern shows two weak and broad peaks between 10° and 80° (Figure S1d, Supporting Information), suggesting the amorphous nature or low crystallization of the as-prepared Fe(OH)₃. The relatively low synthesis temperature (room temperature) is responsible for the low crystallinity of Fe(OH)₃. A panoramic view (Figure S1e, Supporting Information) reveals that Fe(OH)₃ hierarchical nanotubes are consisted of uniform hierarchical 1D nanostructures without impurities or aggregates. The diameter of 1D nanostructure increases from ≈ 100 to ≈ 145 nm after reaction (Figure S1f, Supporting Information). The inner cavity is clearly revealed by the obvious contrast between solid shell and hollow interior in Figure S2 (Supporting Information). The diameter of hollow interior is ≈ 120 nm with 1D structure hierarchies' nanorods pointing outward (Figure 1g). All this confirms that hierarchical nanotube well duplicates 1D structure and no structural degradation occurs. Additionally, hydrolysis rate of Fe²⁺ plays a crucial role in the formation of the hierarchical nanotubes. When mixed solvent is replaced by pure ethanol, hydrolysis rate of Fe²⁺ is significantly reduced. As a result, MnOOH nanowires remain largely unreacted (Figure S4a,b, Supporting Information). When mixed solvent is replaced by pure water, the hydrolysis of Fe³⁺ is significantly accelerated. Due to the fast hydrolysis rate, nanosheets rather than nanorods are formed (Figure S4c,d, Supporting Information). This suggests that the morphology of the tubular structures could be tuned by varying the composition of the solvent.^[38]

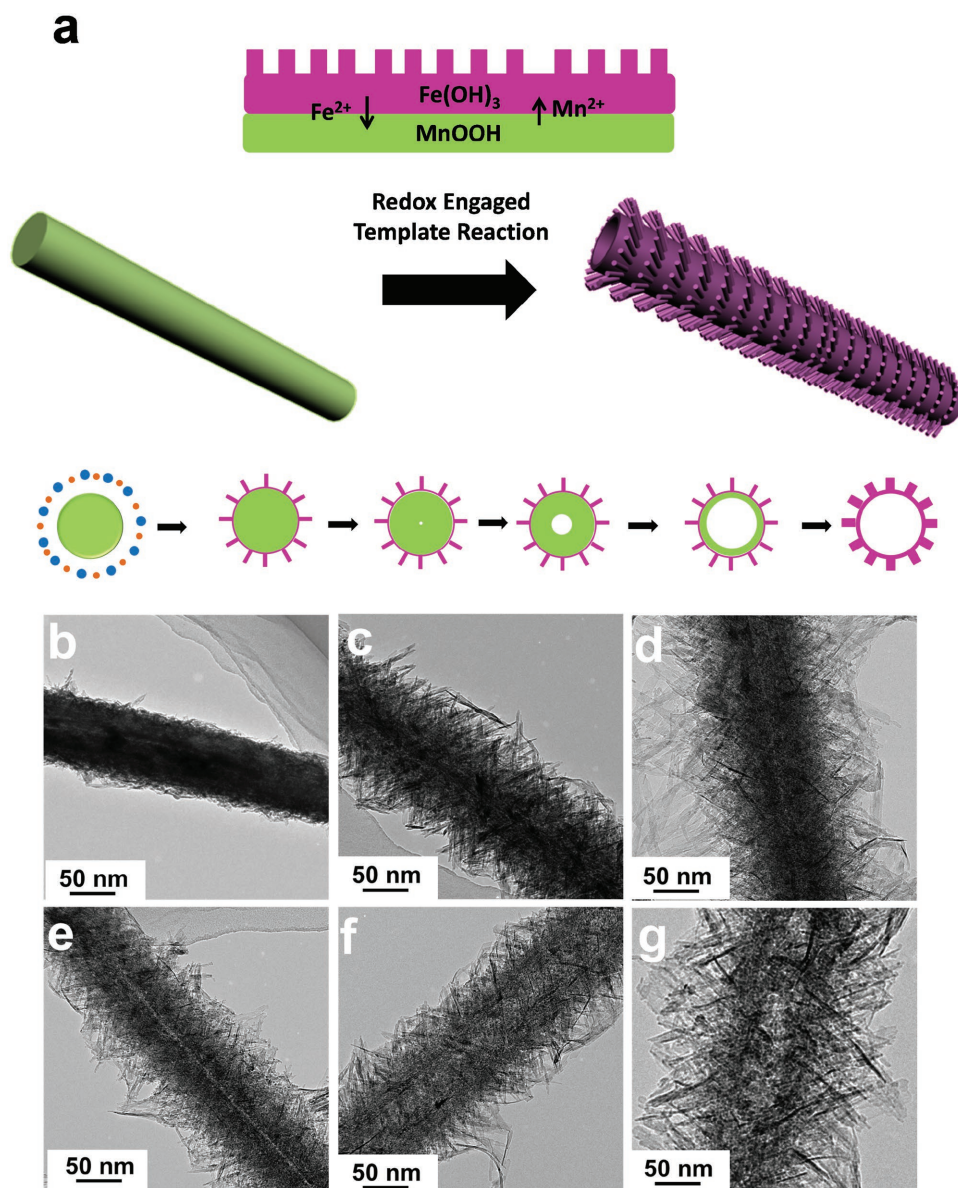


Figure 1. a) Schematic illustrations of the formation process. b–g) TEM images of the products with different reaction durations: 10 min (b), 30 min (c), 1 h (d), 2 h (e), 6 h (f), and 12 h (g), respectively.

The morphological evolution of Fe(OH)₃ hierarchical nanotubes as precursor during annealing process is also investigated. Through controlling the annealing temperature, various 1D α -Fe₂O₃ nanostructures including hierarchical nanotubes at 500 and 600 °C (α -Fe₂O₃-500 and α -Fe₂O₃-600), porous nanotubes at 700 °C (α -Fe₂O₃-700), and ladder-like nanostructures at 800 °C (α -Fe₂O₃-800), are obtained (Figure 2). After annealing, all XRD patterns (Figure S5, Supporting Information) reveal the formation to α -Fe₂O₃ as evidenced by the pronounced diffraction peaks, especially the (1 0 4), (1 1 0), and (1 1 6) peaks from hematite Fe₂O₃ (JCPDS 24-0072) in Figure S5 (Supporting Information). When annealed at 500 °C, uniform hierarchical nanotubes with no apparent collapse are obtained (Figure 2e,i), indicating that the hierarchical nanotubes are able to withstand

the thermal annealing at 500 °C. Due to the unique hollow structure and small crystallite size, α -Fe₂O₃-500 possesses a large Brunauer–Emmett–Teller (BET) surface area of 88.5 m² g⁻¹ and a mesopore size of around 10 nm (Figure S6a, Supporting Information). With the elevation of annealing temperature to 600 °C, nanorod building blocks on the shell grow into nanoparticles. As a result, larger pores can be easily observed on the shell of the tubular structure (Figure 2f,j). The surface area decreases to 33.2 m² g⁻¹ and pore size increases to around 50 nm (Figure S6b, Supporting Information). Further increase of annealing temperature to 700 °C results in further crystal growth and the disappearance of rough nanoparticles on the surface. The original mesopores merge together, forming interconnected large pores on the shell of

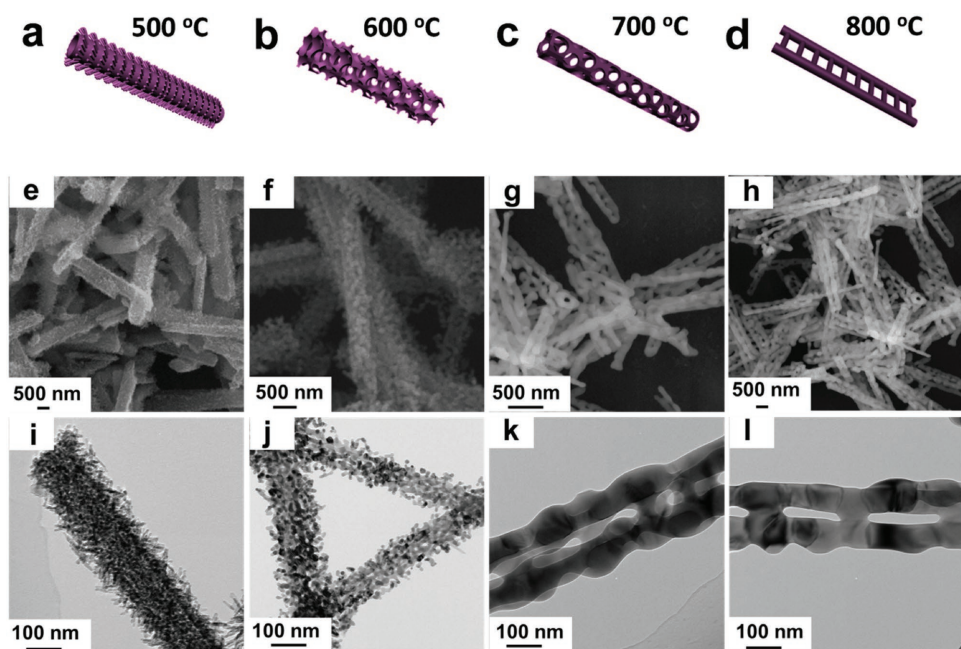


Figure 2. Schematic illustrations, SEM images, and TEM images of a,e,i) α -Fe₂O₃-500, b,f,j) α -Fe₂O₃-600, c,g,k) α -Fe₂O₃-700, and d,h,l) α -Fe₂O₃-800.

tubular structure (Figure 2g,k). The surface area further drops to 13.0 m² g⁻¹ with no obvious pores below 100 nm (Figure S6c, Supporting Information). Another increase of annealing temperature to 800 °C results in the formation of ladder-like nanostructures, consisted of two long sides crossed by parallel rungs (Figure 2h,l). The surface area of the sample decreases to 8.5 m² g⁻¹ (Figure S6d, Supporting Information). For α -Fe₂O₃-500 and α -Fe₂O₃-600, a hysteresis loop at a higher pressure ($P/P_0 = 0.90$ - 0.99) probably reveals the interchannel macroporous caused from structural defects, while for α -Fe₂O₃-700 and α -Fe₂O₃-800, no obvious hysteresis loop at a higher pressure ($P/P_0 = 0.90$ - 0.99) is observed, indicating less structural defects.^[48] Additionally, the high-resolution transmission electron microscopy (HRTEM) images of α -Fe₂O₃-500, α -Fe₂O₃-600, α -Fe₂O₃-700, and α -Fe₂O₃-800 all show the same lattice fringes of 3.6 Å, corresponding to the (0 1 2) lattice plane (Figure S7, Supporting Information).

It is found that upon annealing, the peaks become sharper as a result of an increase in crystallite size and the loss of internal strains (Figure S8, Supporting Information). Thus, crystal structure change of the four different samples is further investigated by using Rietveld refinement. According to the refinement, the crystallite size increases while the strain decreases with the annealing temperature increasing (Table S3, Supporting Information). Our result shows that large strain corresponds to small particles, which is consensus to the previous reports.^[49,50] We further investigate defects in the annealing process by refining the atomic occupancies. The absence of oxygen release upon heating rules out the possibility of anionic excess.^[49] Thus, it is found that the formulas of α -Fe₂O₃-500, α -Fe₂O₃-600, α -Fe₂O₃-700, and α -Fe₂O₃-800 are [Fe_{0.9834}□_{0.0166}]O_{1.5}, [Fe_{0.9852}□_{0.0147}]O_{1.5}, [Fe_{0.9868}□_{0.0132}]O_{1.5}, and [Fe_{0.9906}□_{0.0094}]O_{1.5}, respectively, suggesting a slight nonstoichiometry and α -Fe₂O₃-800

is the most approaching the stoichiometry. Two types of defects should thus be taken into account to explain our data. The first one deals with cation vacancies, which can enlist either iron vacancies leading to an oxygen rich structure or the departure of two ions of opposite charge (Schottky defects). In contrast, the second one involves an interstitial cation (Frenkel defects) displaced from its initial position and leading to a vacancy (Figure S9, Supporting Information).^[49] It is known that α -Fe₂O₃ crystallizes in a structure that consists of a distorted hexagonally closest packed layer sequence of oxygen with iron occupying two-thirds of the octahedral holes (Figure S10, Supporting Information). Thus, vacancy of Fe would locate in [FeO₆] octahedral holes.^[51] For α -Fe₂O₃-500, the refined cell parameter ($a = 5.044$ Å) is slightly higher than the ideal values ($a = 5.038$ Å), while the occupation of Fe atom is lower than the ideal value, indicating a loss of compactness in the atomic arrangement, in agreement with the existence of Frenkel defects and surface relaxation effects.^[49,52] (Figure S9, Supporting Information). However, for α -Fe₂O₃-600 and α -Fe₂O₃-700, the refined cell parameter and occupation of Fe atom are both lower than the ideal values (Figure S10, Supporting Information). The lattice volume decreases with increasing particle size as well as the elevating temperature up to 700 °C. This opposite situation against α -Fe₂O₃-500 indicates that the defect is dominated by Schottky disorder.^[50] When the temperature is increased to 800 °C, the lattice volume is increased and is approaching the ideal value while the Fe occupation is also approaching 1, suggesting the lowest defect density. This phenomenon is attributing to both Frenkel defects and Schottky defects which are largely reduced and α -Fe₂O₃-800 shows good lattice coherency.^[53] Thus, more Frenkel defects dominates at low annealing temperature, while the high annealing temperature would lead to Schottky disorder in domination^[50,53] while

the total defect density is decreasing. Combining the results of the microscopic view and the XRD refinement results, we can conclude that large crystals are formed by the assembly and migration of the polycrystalline small iron oxide domains, leading to the low surface area upon annealing. Pore migration is observed after thermal treatment from mesopores to macropores, during which small iron oxide domains move, coalesce and eventually lead to the disappearance of hierarchies. Intrinsic surface stresses on 1D nanostructure result in growth of ladder-like nanostructure. The observed ladder-like nanostructure arises from pore migrations with crystal lattice rearrangement. The grain boundary on 1D framework migrates due to tensile stress, leading to stress relaxation. Thus, α -Fe₂O₃-800 is formed by the relaxation of mechanical stresses and confined growth of α -Fe₂O₃ on the 1D framework. Furthermore, high-temperature annealing could also reduce defect density and improve lattice coherency. In this way, interparticle contacts and/or the contacts at the interphase of α -Fe₂O₃ are well improved which are also consensus to the results of TEM

(Figure S7, Supporting Information), and promise the stable structure integrity.^[54]

Motivated by the high lithium storage capacity of hematite, we evaluated the electrochemical properties by taking α -Fe₂O₃-500 and α -Fe₂O₃-800 as examples. Figure 3a shows the representative cyclic voltammograms (CVs) for the initial three cycles at a scan rate of 0.1 mV s⁻¹ in voltage range of 0.01–3.0 V. During the first cathodic sweep, the dominant reduction peak at \approx 0.52 V is attributed to lithium insertion and subsequent reduction of α -Fe₂O₃ according to the conversion reaction ($\text{Fe}_2\text{O}_3 + 6\text{Li}^+ + 6\text{e}^- \rightarrow 2\text{Fe} + 3\text{Li}_2\text{O}$) as well as the formation of SEI layer.^[38] The decrease in peak intensity in the subsequent scans indicate irreversible formation of SEI layer during the first cycle. The redox peaks for the second and third cycles overlap quite well, indicating excellent reversibility of the electrochemical reaction. Figure 3b illustrates cycling performances of α -Fe₂O₃-500 and α -Fe₂O₃-800 at 100 mA g⁻¹. α -Fe₂O₃-800 delivers high first-cycle discharge and charge capacities of 1377 and 1102 mA h g⁻¹, respectively,

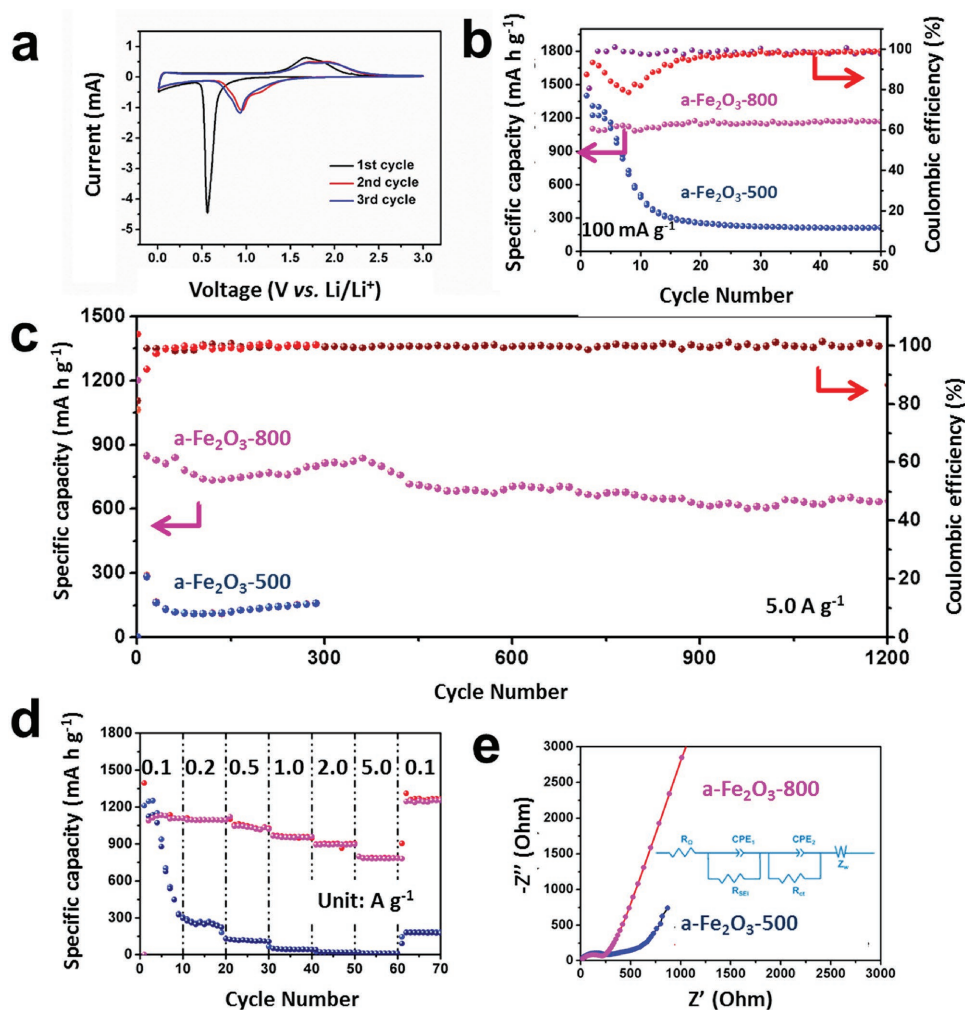


Figure 3. a) CV curves of α -Fe₂O₃-800 at 0.1 mV s⁻¹. b) Cycling performance of the α -Fe₂O₃-800 and α -Fe₂O₃-500 at 100 mA g⁻¹. c) High-rate cycling performance of the α -Fe₂O₃-800 and α -Fe₂O₃-500 at 5.0 A g⁻¹. d) Rate performance of the α -Fe₂O₃-800 and α -Fe₂O₃-500. e) AC impedance response of the α -Fe₂O₃-800 and α -Fe₂O₃-500 at open circuit potential.

corresponding to an irreversible loss of 20%, which is mainly ascribed to irreversible side reactions on the surface including the formation of the SEI layer and the possible incomplete restoration of metallic Fe into the original oxide. The reversible discharge capacity reaches 1200 mA h g^{-1} after 50 cycles.^[38] In sharp contrast, rapid capacity decay has been observed for $\alpha\text{-Fe}_2\text{O}_3\text{-500}$. Although $\alpha\text{-Fe}_2\text{O}_3\text{-500}$ shows higher initial discharge capacity (1399 mA h g^{-1}), capacity quickly degrades to around 211 mA h g^{-1} . The capacity retention versus second cycle capacity is only 17.3%. Noteworthy, Coulombic efficiency (CE) also differs greatly in each sample. $\alpha\text{-Fe}_2\text{O}_3\text{-800}$ shows stable CEs above 98.5% ever since the second cycle. On the contrast, $\alpha\text{-Fe}_2\text{O}_3\text{-500}$ exhibits extremely low CEs in the initial 20 cycles and the lowest CE reaches 78% at the eighth cycle. The difference in cycling performance and CE demonstrates the superior reversibility of $\alpha\text{-Fe}_2\text{O}_3\text{-800}$.^[9]

Stable cycling performance is also achieved at a high specific current of 5.0 A g^{-1} . $\alpha\text{-Fe}_2\text{O}_3\text{-800}$ delivers a reversible capacity of 645 mA h g^{-1} even after 1200 cycles, resulting in a capacity fading of 0.027% per cycle against second cycle. To the best of our knowledge, this is the best cycle performance reported for $\alpha\text{-Fe}_2\text{O}_3$ anode materials. Note that this performance is achieved by pristine iron oxide without the modification of carbon. In contrast, $\alpha\text{-Fe}_2\text{O}_3\text{-500}$ shows high initial capacity of 1142 mA h g^{-1} , capacity quickly degrades to around 110 mA h g^{-1} after 80 cycles. The rapid capacity fading is accompanied by low CE. After 45 cycles, both capacity and CE begin to stabilize, while the capacity afterward is too low for practical use. Figure 3d shows the rate performance of $\alpha\text{-Fe}_2\text{O}_3\text{-800}$ and $\alpha\text{-Fe}_2\text{O}_3\text{-500}$. $\alpha\text{-Fe}_2\text{O}_3\text{-800}$ exhibits reversible capacities of 1128, 1094, 1033, 949, 897, and 783 mA h g^{-1} at the step increase specific currents of 0.1, 0.2, 0.5, 1.0, 2.0, and 5.0 A g^{-1} , respectively. After cycling at various specific currents, a specific capacity as high as 1244 mA h g^{-1} is well recovered at a specific current of 0.1 A g^{-1} . No capacity decay is observed when compared to capacity at the same current before high rate testing. While for $\alpha\text{-Fe}_2\text{O}_3\text{-500}$, only 1/10 of second capacity can be recovered and the capacity at each specific current is obviously lower. The outstanding rate performance confirms the excellent Li^+ storage reversibility of $\alpha\text{-Fe}_2\text{O}_3\text{-500}$ even at high rate. The electrochemical impedance spectrum (EIS) of $\alpha\text{-Fe}_2\text{O}_3\text{-800}$ shows a compressed semicircle from the high to medium frequency range of each spectrum, and a line inclined at $\approx 45^\circ$ in low-frequency range (Figure 3e). The smaller diameter of the semicircle for $\alpha\text{-Fe}_2\text{O}_3\text{-800}$ electrode in the mid-frequency region ($10^1\text{--}10^4 \text{ Hz}$) suggests a reduced charge transfer resistance when compared to the $\alpha\text{-Fe}_2\text{O}_3\text{-500}$.

$\alpha\text{-Fe}_2\text{O}_3\text{-800}$ and $\alpha\text{-Fe}_2\text{O}_3\text{-500}$ were further subjected to different discharge–charge cycles. The capacity failure of $\alpha\text{-Fe}_2\text{O}_3\text{-500}$ is observed in approximately ten cycles. Thus, we choose the first cycle and tenth cycle as representative to characterize the morphology and structure. The resulting structures and AC impedance responses were characterized by SEM, TEM, and EIS, respectively. During the first cycle discharge to 0.01 V, both samples exhibit rather rough surface (Figures S11 and S12, Supporting Information). When recharged to 3.0 V, $\alpha\text{-Fe}_2\text{O}_3\text{-800}$ shows no obvious structure change (Figure S13, Supporting Information). The surface is smooth, indicating the formation of a thin SEI layer on the surface (Figure S14a,b, Supporting

Information). For $\alpha\text{-Fe}_2\text{O}_3\text{-500}$, nanorod hierarchies disappear and surface becomes rather rough after one discharge–charge cycle (Figure S14e,f, Supporting Information), suggesting the formation of a thick SEI layer on the surface. The difference gets greater after ten cycles. $\alpha\text{-Fe}_2\text{O}_3\text{-800}$ maintains excellent structural integrity with a limited SEI layer on their surfaces (Figure S14c,d, Supporting Information). On the contrary, $\alpha\text{-Fe}_2\text{O}_3\text{-500}$ is buried in the thick SEI layer and shows no sign of the original 1D structure remains (Figure S14g,h, Supporting Information). The unstable structure of $\alpha\text{-Fe}_2\text{O}_3\text{-500}$ leading to excessive SEI formation is the primary reason for the rapid capacity fading, and CEs. $\alpha\text{-Fe}_2\text{O}_3\text{-800}$ with the least internal strain and defects enables an outstandingly stable battery performance and high-power rate capability. It is believed that nonuniform strain or residual stress of $\alpha\text{-Fe}_2\text{O}_3$ lattice would result in disorder and distortion of the $\alpha\text{-Fe}_2\text{O}_3$ matrix, and during charging/discharging and with the strain development, finally the pulverization of electrode is achieved.

Furthermore, we carried out the HRTEM images of the $\alpha\text{-Fe}_2\text{O}_3\text{-500}$ and $\alpha\text{-Fe}_2\text{O}_3\text{-800}$ after ten cycles (Figure 4). Both $\alpha\text{-Fe}_2\text{O}_3\text{-500}$ and $\alpha\text{-Fe}_2\text{O}_3\text{-800}$ are composed of small particles. In order to obtain further information, Selected Area Electron Diffraction (SAED) pattern is obtained in Figure 4c,f. Both patterns show polycrystalline nature. While the lattice fringes of (1 1 1), (2 0 0), and (2 2 0) planes of Li_2O (JCPDS 77-2144) and those of (1 0 4), (1 1 3), and (1 1 6) of $\alpha\text{-Fe}_2\text{O}_3$ (JCPDS 01-1053) are very similar, it is very important to figure out the specific lattice fringes of (0 1 2), (0 2 4), and (1 0 10) of $\alpha\text{-Fe}_2\text{O}_3$ as well as the specific lattice fringe of (2 0 0) of Li_2O . The SAED pattern of $\alpha\text{-Fe}_2\text{O}_3\text{-800}$ is shown in Figure 4c. The d-spacings of 2.69 and 2.20 \AA determined from the pattern are consistent with the lattice fringes of the (1 0 4) and (1 1 3) planes of $\alpha\text{-Fe}_2\text{O}_3$ (JCPDS 01-1053). All diffraction rings of ladder-like nanostructure in Figure 4c can be well indexed as the rhombohedral phase of $\alpha\text{-Fe}_2\text{O}_3$ (JCPDS 01-1053). No diffraction rings of Li_2O and Fe are found. The SAED pattern of $\alpha\text{-Fe}_2\text{O}_3\text{-500}$ is shown in Figure 4f. Three bright lattice fringes correspond to mixed lattice fringes of (0 1 2), (0 2 4), and (1 0 10) of $\alpha\text{-Fe}_2\text{O}_3$ as well as (1 1 1), (2 0 0), and (2 2 0) planes of Li_2O . The specific lattice fringes of (0 1 2), (0 2 4), and (1 0 10) of $\alpha\text{-Fe}_2\text{O}_3$ can be easily figured out while lattice spacing of (2 0 0) of Li_2O is also observed, indicating the existence of both $\alpha\text{-Fe}_2\text{O}_3$ and Li_2O . Two bright symmetrical points are observed and are in well accordance to lattice fringe of (1 1 0) plane body-centered cubic Fe (JCPDS 87-0722). It is worth noting that the lattice fringes of $\alpha\text{-Fe}_2\text{O}_3$ and that of Fe are all very weak when compared to that of Li_2O and those of the mixed lattice fringes. These phenomena may be linked to that Fe and $\alpha\text{-Fe}_2\text{O}_3$ both are embedded in the Li_2O matrix as well as SEI layer and in this way, the diffraction intensity is largely weakened. Normally, thermodynamically irreversible extraction of Li from Li_2O would cause a capacity loss during the transformation of Fe^0 to Fe^{3+} . However, it did not occur in the case of ladder-like nanostructure, indicating the enhanced reversibility of conversion reaction in $\alpha\text{-Fe}_2\text{O}_3\text{-800}$.

Ex situ EIS results provide further insights in the formation of SEI layer (Figure S14e,f, Supporting Information). Table S4 (Supporting Information) gives the fitting value of $\alpha\text{-Fe}_2\text{O}_3\text{-800}$ and $\alpha\text{-Fe}_2\text{O}_3\text{-500}$. Both $\alpha\text{-Fe}_2\text{O}_3\text{-800}$ and the $\alpha\text{-Fe}_2\text{O}_3\text{-500}$ show

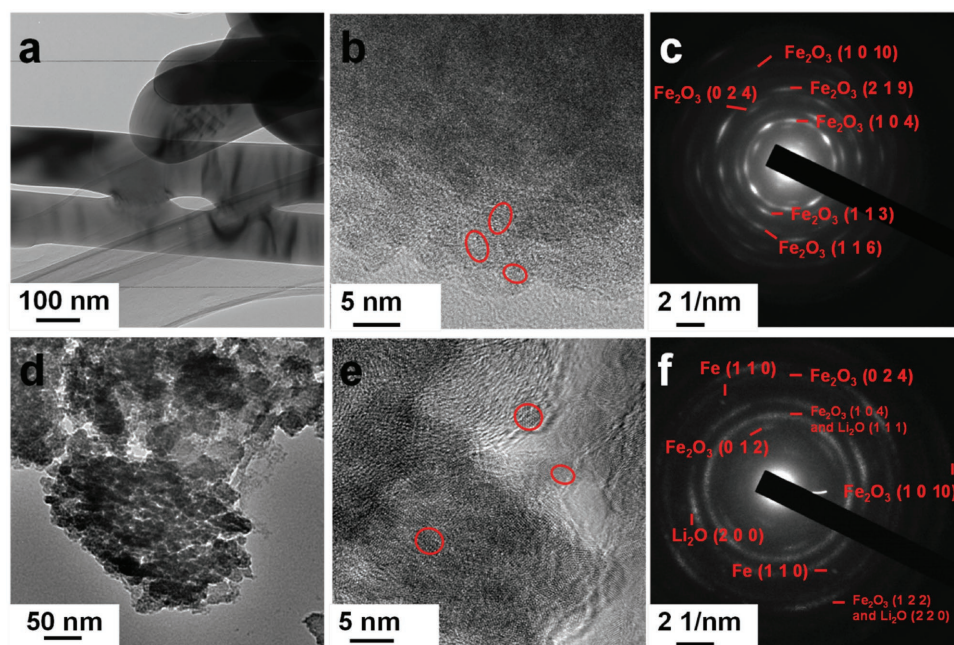


Figure 4. a,b) TEM images of α -Fe₂O₃-800 after ten cycles. c) The corresponding SAED pattern of α -Fe₂O₃-800 after ten cycles. d,e) TEM images of α -Fe₂O₃-500 after ten cycles. f) The corresponding SAED pattern of α -Fe₂O₃-500 after ten cycles.

extreme low charge transfer resistances, while the resistance related to SEI layer of α -Fe₂O₃-500 is a bit higher than that of the α -Fe₂O₃-800. However, the difference gets greater after ten cycles (Table S4, Supporting Information). For the α -Fe₂O₃-800, it is found that during the first ten cycles, only small increase in charge transfer resistance from 2.4 to 4.7 Ω and no increase in the resistance related to SEI layer are observed, indicating the stable SEI layer. On the contrast, for α -Fe₂O₃-500, the charge transfer resistance is increased to 113.5 Ω and the resistance related to SEI layer is increased to 184.3 Ω . This phenomenon indicates that upon charging/discharging, SEI layer is formed intensively for α -Fe₂O₃-500, leading to the higher resistance related to SEI layer. In addition, thick SEI layer also retard the electron transport, leading to the low capacity and undesirable cycling performance.^[9,55,56]

To further investigate the influence of thermal induced strain relaxation on the electrochemical performance, we evaluated the cycling performance of α -Fe₂O₃-500, α -Fe₂O₃-600, α -Fe₂O₃-700, and α -Fe₂O₃-800 at 2 A g⁻¹ (Figure S15, Supporting Information). The initial discharge capacity of the first cycle decreases with the increase of annealing temperature from 500 to 800 °C (Figure S16, Supporting Information). It is interesting to find that the surface area versus capacity follows well-fitted linear relationship (Figure S17, Supporting Information). To be more precise, the total specific capacity of Fe₂O₃ during the first discharge can be calculated from the equation below^[57]

$$C_{\text{total}} = C_{\text{conversion}} + C_{\text{interface}} + C_{\text{surface}} + C_{\text{SEI}} \quad (1)$$

where C_{total} , $C_{\text{conversion}}$, $C_{\text{interface}}$, C_{surface} , and C_{SEI} are, respectively, the total specific capacity, conversion reaction capacity, interfacial storage capacity, surface capacities from reversible reaction of LiOH to form LiH, and the SEI formation

capacities.^[57] $C_{\text{interface}}$ and C_{SEI} are largely associated with the surface area, while $C_{\text{conversion}}$ and C_{surface} are not directly linked to surface area. Thus, it is no surprising that the first discharge capacity follows linear relationship with the surface area in our case. Furthermore, capacity failure is observed in α -Fe₂O₃-700, α -Fe₂O₃-600, and α -Fe₂O₃-500, while α -Fe₂O₃-800 shows stable cycling performance without capacity failure for 400 cycles. The cycling failure of α -Fe₂O₃-700, α -Fe₂O₃-600, and α -Fe₂O₃-500 is located in 10th, 20th, and 40th cycles, respectively (Figure S15, Supporting Information). The capacity retention against the second cycle is also increased from 38% to 89%, indicating that the higher temperature results in more stable cycling stability. To further identify the interphase between the electrolyte and electrode, EIS of these 1D nanostructures is carried out. The R_{ct} value decreases with the rising of the annealing temperature, indicating that through thermally induced strain relaxation, charge transfer is well facilitated (Figure S18, Supporting Information). This is related to the reduced surface defect, leading to stable electrode/electrolyte interphase. The capacity failure occurs due to the nonuniform strain or residual stress of α -Fe₂O₃-700, α -Fe₂O₃-600, and α -Fe₂O₃-500 which have a severe scattering effect on the transport of charges.^[58] This would result in disorder and distortion of the Fe₂O₃ matrix, finally collapse. During charging/discharging, with the strain development, finally pulverization of electrode is achieved. However, for α -Fe₂O₃-800, good lattice coherency and stable particle contact are able to buffer the volume expansion during cycling. In this way, excellent cycling stability is achieved (Figure 5).

Overall, our results show the double-edged influence of high surface area in the battery performance. On one hand, it leads to more active sites contributing higher capacity. On the other hand, it also brings about more defects, which are hazardous to

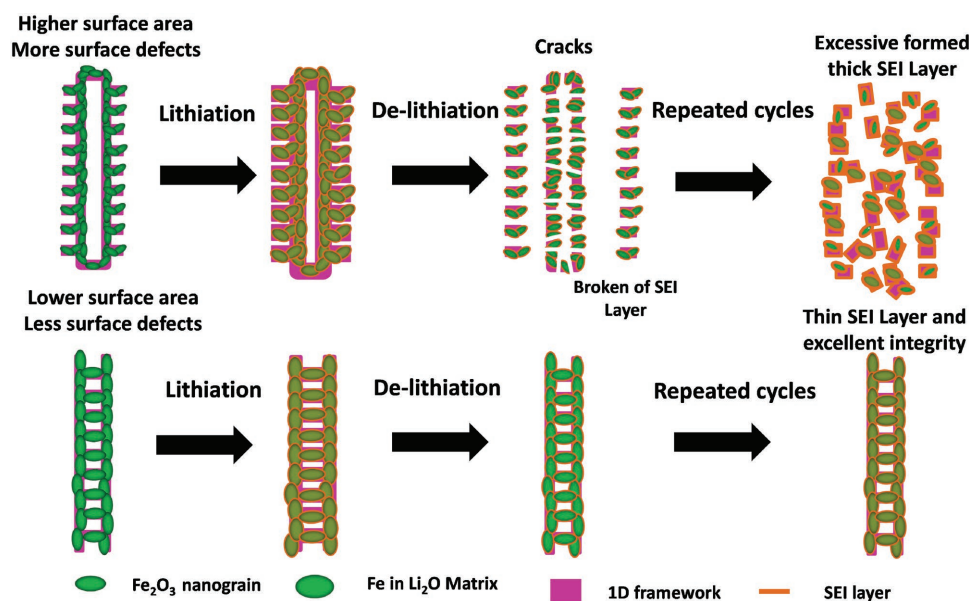


Figure 5. Schematic illustration of morphology evolution and SEI formation of α -Fe₂O₃-800 and α -Fe₂O₃-500 during discharge/charge cycling.

the structural integrity and unstable interphase between electrode and electrolyte, especially during charging/discharging, leading to quick capacity fading. In this way, thermal induced strain relaxation would offer advantages below: first, the internal strain is relaxed and the defect is reduced, resulting in good interparticle contacts and the electrode is able to stand the volume expansion/expansion without mechanical breaking. Second, the resultant stable nanostructure allows for the development of a thin and stable SEI. Third, with the least lattice strain left, the good lattice coherency would result in stable electrode/electrolyte interphase and facilitates the transport of charge, avoiding the scattering effect. In this way, α -Fe₂O₃-800 with most stable morphology shows excellent electrochemical performance.^[33,49] In addition, it is found that the first discharge capacity follows linear relationship with the surface area in our case which is associated with the interfacial capacity and SEI formation.^[59]

3. Conclusions

We for the first time propose thermal induced strain relaxation to realize the stable SEI control without the additional protective strategy. α -Fe₂O₃-800, as an example, has been fabricated through a template-engaged redox reaction followed by thermal treatment. The thermal treatment induces interfacial atomic rearrangement and results in the formation of a series of 1D nanostructure. It is demonstrated that through thermal treatment, grain boundary is reduced, lattice strain is largely relaxed, and defect density is well reduced, improving the interparticle contacts and contact at the interface of electrode, stabilizing the electrode/electrolyte interphase, facilitating the charge transfer. In this way, α -Fe₂O₃-800 is able to withstand the volume change upon charging/discharging without mechanical breaking and leads to a thin and stable SEI formation. As a result, the

ladder-like α -Fe₂O₃ nanostructures obtained at 800 °C deliver an outstanding stable capacity of 1200 mA h g⁻¹ at 100 mA g⁻¹ and an excellent high-rate cyclability with a capacity fading of 0.056% per cycle for 1200 cycles at 5 A g⁻¹. We believe the strategy of thermal induced strain relaxation would expand to other high-capacity anode and cathode material systems that undergo large volume expansion, which are promising for applications in energy storage and conversion.

4. Experimental Section

Preparation of the Fe(OH)₃ Hierarchical Nanotubes: The MnOOH nanowires were fabricated through the method reported before. 2 mmol of MnOOH nanowire was dispersed in 40 mL alcohol for 30 min to form solution A. 3 mmol FeSO₄·7H₂O was dissolved in 70 mL water to form solution B. The solution B was added into solution A dropwise and reacted for 12 h at room temperature. The precipitation was then collected and washed with deionized water and alcohol for several times to obtain Fe(OH)₃ hierarchical nanotubes.

Preparation of Various α -Fe₂O₃ 1D Structures: The Fe(OH)₃ hierarchical nanotubes were used as precursor to anneal in the air at different temperatures for 5 h. Hierarchical nanotubes were obtained at 500 and 600 °C, porous nanotubes at 700 °C, and ladder-like nanostructures at 800 °C.

Material Characterization: The crystal structure change of the four different samples was investigated by using Rietveld refinement. To avoid the fluorescence effect and ensure high resolution pattern, the light source was changed from Cu K α (λ = 1.788 Å) to Co K α (λ = 1.788 Å). X-ray powder diffraction measurements were performed on the D8 Discovery diffractometer (Bruker AXS, Karlsruhe, Germany) with a goniometer radius 217.5 mm. XRD patterns were recorded with the following measurement conditions: tube voltage of 40 kV, tube current of 40 mA, a coupled 2 θ mode with three graphs, and each graph taken for 600 s. The X-ray diffractograms were analyzed using software TOPAS 4.2. The refinement procedure in TOPAS 4.2 assumed a repeated minimization from random starting values, which were obtained through the TOPAS keywords: "continue after convergence" (which meant the refinement was carried out until a certain iteration number, despite

the convergence had been locally reached) and “randomize on errors” (meaning that the starting values were taken randomly as a function of the errors). The microstructures were observed by field-emission scanning electron microscopy (JEOL-7100F), and transmission electron microscopy and HRTEM (JEM-2100F). BET surface areas were measured by using Tristar II 3020 instrument.

Electrochemical Characterization: The electrochemical properties were characterized by assembly of CR2016-type coin cells with lithium metal foil as the anode in a glovebox filled with pure argon gas. The cathode electrodes were composed of 60% active material, 30% acetylene black, and 10% sodium alginate binder. Copper foil was used as collector for the coating. A solution (1 M) of LiPF₆ in Ethylene Carbonate/Dimethyl Carbonate (1:1 vol/vol) was used as the electrolyte. The cells were aged for 12 h before charge/discharge process to ensure full filtration of the electrolyte into the electrodes. The capacity was calculated based on the total mass of the composite. The mass loading of each electrode was 1.5–2.0 mg cm⁻². Galvanostatic charge/discharge measurement was performed by a multichannel battery testing system (LAND CT2001A), cyclic voltammetry (0.01–3 V) was performed using an electrochemical workstation (CHI 760S), EIS was tested with an Autolab potentiostat galvanostat (PGSTAT302N). The EIS was carried out at frequency range from 0.1 to 10 000 Hz at open circuit potential before cycling to avoid the influence of Li metal. All the measurements were carried out at room temperature. In order to prepare the SEM images after cycling, the electrode was taken out of the disassembled cell and soaked immediately in acetone for 24 h for washing the residue of electrolytes. The samples after cycling were detached and dispersed in the alcohol to form suspension. The suspension was dropped on the aluminum foil and dried for SEM characterization.

Supporting Information

Supporting Information is available from the Wiley Online Library or from the author.

Acknowledgements

K.N.Z., M.Y.W., and Y.F.D. contributed equally to this work. This work was supported by the National Key Research and Development Program of China (2016YFA0202603), National Basic Research Program of China (2013CB934103), the International Science & Technology Cooperation Program of China (2013DFA50840), the National Natural Science Foundation of China (51302203, 51272197, 51521001), the National Science Fund for Distinguished Young Scholars (51425204), the Hubei Science Fund for Distinguished Young Scholars (2014CFA035), and the Fundamental Research Funds for the Central Universities (2015-III-021, 2015-III-032, 2015-III-052, 2015-PY-2). The authors are deeply thankful to Professor Dongyuan Zhao of the Fudan University, and Dr. Jun Liu of the Pacific Northwest National Laboratory for their stimulating discussion and kind help.

Received: July 20, 2016

Published online:

- [1] K. Zhao, L. Zhang, R. Xia, Y. Dong, W. Xu, C. Niu, L. He, M. Yan, L. Qu, L. Mai, *Small* **2015**, *12*, 588.
- [2] Z. Hu, Z. Zhu, F. Cheng, K. Zhang, J. Wang, C. Chen, J. Chen, *Energy Environ. Sci.* **2015**, *8*, 1309.
- [3] K. Zhao, F. Liu, C. Niu, W. Xu, Y. Dong, L. Zhang, S. Xie, M. Yan, Q. Wei, D. Zhao, L. Mai, *Adv. Sci.* **2015**, *5*, 1500154.
- [4] S. Chu, A. Majumdar, *Nature* **2012**, *488*, 294.
- [5] D. Larcher, J.-M. Tarascon, *Nat. Chem.* **2015**, *7*, 11.
- [6] K. Cao, L. Jiao, H. Liu, Y. Liu, Y. Wang, Z. Guo, H. Yuan, *Adv. Energy Mater.* **2015**, *5*, 1401421.
- [7] N. Zhang, X. Han, Y. Liu, X. Hu, Q. Zhao, J. Chen, *Adv. Energy Mater.* **2015**, *5*, 1401123.
- [8] L. Zhang, H. B. Wu, X. W. D. Lou, *Adv. Energy Mater.* **2014**, *4*, 1300958.
- [9] S. H. Lee, S.-H. Yu, J. E. Lee, A. Jin, D. J. Lee, N. Lee, H. Jo, K. Shin, T.-Y. Ahn, Y.-W. Kim, H. Choe, Y.-E. Sung, T. Hyeon, *Nano Lett.* **2013**, *13*, 4249.
- [10] S. Xu, C. M. Hessel, H. Ren, R. Yu, Q. Jin, M. Yang, H. Zhao, D. Wang, *Energy Environ. Sci.* **2014**, *7*, 632.
- [11] J. Zhang, K. Wang, Q. Xu, Y. Zhou, F. Cheng, S. Guo, *ACS Nano* **2015**, *9*, 3369.
- [12] C. Wang, H. Wu, Z. Chen, M. T. McDowell, Y. Cui, Z. Bao, *Nat. Chem.* **2013**, *5*, 7.
- [13] D. Lin, Z. Lu, P.-C. Hsu, H. R. Lee, N. Liu, J. Zhao, H. Wang, C. Liu, Y. Cui, *Energy Environ. Sci.* **2015**, *8*, 2371.
- [14] L. Zhou, H. Xu, H. Zhang, J. Yang, S. B. Hartono, K. Qian, J. Zou, C. Yu, *Chem. Commun.* **2013**, *49*, 8695.
- [15] H. Zhang, X. Sun, X. Huang, L. Zhou, *Nanoscale* **2015**, *7*, 3270.
- [16] W. Xu, K. Zhao, C. Niu, L. Zhang, Z. Cai, C. Han, L. He, T. Shen, M. Yan, L. Qu, L. Mai, *Nano Energy* **2014**, *8*, 196.
- [17] L. Zhang, K. Zhao, W. Xu, Y. Dong, R. Xia, F. Liu, L. He, Q. Wei, M. Yan, L. Mai, *Phys. Chem. Chem. Phys.* **2015**, *17*, 5.
- [18] H. Zhang, L. Zhou, O. Noonan, D. J. Martin, A. K. Whittaker, C. Yu, *Adv. Funct. Mater.* **2014**, *24*, 4337.
- [19] C. Niu, J. Meng, X. Wang, C. Han, M. Yan, K. Zhao, X. Xu, W. Ren, Y. Zhao, L. Xu, Q. Zhang, D. Zhao, L. Mai, *Nat. Commun.* **2015**, *6*, 7402.
- [20] C. Han, M. Yan, L. Mai, X. Tian, L. Xu, X. Xu, Q. An, Y. Zhao, X. Ma, J. Xie, *Nano Energy* **2013**, *2*, 916.
- [21] L. Mai, X. Tian, X. Xu, L. Chang, L. Xu, *Chem. Rev.* **2014**, *114*, 11828.
- [22] Y. F. Dong, S. Li, K. N. Zhao, C. H. Han, W. Chen, B. L. Wang, L. Wang, B. Xu, Q. L. Wei, L. Zhang, X. Xu, L. Q. Mai, *Energy Environ. Sci.* **2015**, *8*, 1267.
- [23] L. Zhang, K. Zhao, W. Xu, J. Meng, L. He, Q. An, X. Xu, Y. Luo, T. Zhao, L. Mai, *RSC Adv.* **2014**, *4*, 3332.
- [24] W. Ren, Z. Zheng, Y. Luo, W. Chen, C. Niu, K. Zhao, M. Yan, L. Zhang, J. Meng, L. Mai, *J. Mater. Chem. A* **2015**, *3*, 19850.
- [25] H. Tan, X. Rui, H. Yu, W. Liu, C. Xu, Z. Xu, H. H. Hng, Q. Yan, *ACS Nano* **2014**, *8*, 4004.
- [26] M.-H. Park, Y. Cho, K. Kim, J. Kim, M. Liu, J. Cho, *Angew. Chem., Int. Ed.* **2011**, *50*, 9647.
- [27] Y.-L. Ding, Y. Wen, C. Wu, P. A. van Aken, J. Maier, Y. Yu, *Nano Lett.* **2015**, *15*, 1388.
- [28] Y. Yu, X. Yin, A. Kvit, X. Wang, *Nano Lett.* **2014**, *14*, 2528.
- [29] G. Zhang, H. B. Wu, H. E. Hoster, X. W. D. Lou, *Energy Environ. Sci.* **2014**, *7*, 302.
- [30] Y. Sun, R. B. Sills, X. Hu, Z. W. Seh, X. Xiao, H. Xu, W. Luo, H. Jin, Y. Xin, T. Li, Z. Zhang, J. Zhou, W. Cai, Y. Huang, Y. Cui, *Nano Lett.* **2015**, *15*, 3899.
- [31] N. Kornienko, D. D. Whitmore, Y. Yu, S. R. Leone, P. Yang, *ACS Nano* **2014**, *9*, 3951.
- [32] M.-H. Liu, Y.-T. Liu, C. R. C. Wang, *Chem. Mater.* **2015**, *27*, 2832.
- [33] B. Kong, J. Tang, C. Selomulya, W. Li, J. Wei, Y. Fang, Y. Wang, G. Zheng, D. Zhao, *J. Am. Chem. Soc.* **2014**, *136*, 6822.
- [34] S. Peng, L. Li, Y. Hu, M. Srinivasan, F. Cheng, J. Chen, S. Ramakrishna, *ACS Nano* **2015**, *9*, 1945.
- [35] J. Nai, Y. Tian, X. Guan, L. Guo, *J. Am. Chem. Soc.* **2013**, *135*, 16082.
- [36] Z. Wang, D. Luan, F. Y. C. Boey, X. W. D. Lou, *J. Am. Chem. Soc.* **2011**, *133*, 4738.
- [37] M. H. Oh, T. Yu, S.-H. Yu, B. Lim, K.-T. Ko, M.-G. Willinger, D.-H. Seo, B. H. Kim, M. G. Cho, J.-H. Park, K. Kang, Y.-E. Sung, N. Pinna, T. Hyeon, *Science* **2013**, *340*, 964.
- [38] G. Gao, L. Yu, H. B. Wu, X. W. D. Lou, *Small* **2014**, *10*, 1741.

- [39] K.-Y. Niu, J. Park, H. Zheng, A. P. Alivisatos, *Nano Lett.* **2013**, *13*, 5715.
- [40] J. Liu, Y. Wen, P. A. van Aken, J. Maier, Y. Yu, *Nano Lett.* **2014**, *14*, 6387.
- [41] Z. Wang, D. Luan, C. M. Li, F. Su, S. Madhavi, F. Y. C. Boey, X. W. D. Lou, *J. Am. Chem. Soc.* **2011**, *132*, 16271.
- [42] Y.-L. Ding, Y. Wen, P. A. van Aken, J. Maier, Y. Yu, *Chem. Mater.* **2015**, *27*, 3143.
- [43] Y.-L. Ding, Y. Wen, P. A. van Aken, J. Maier, Y. Yan, *Nanoscale* **2014**, *6*, 11411.
- [44] J. D. Hem, C. E. Roberson, R. B. Fournier, *Water Resour. Res.* **1982**, *18*, 563.
- [45] J. S. Cho, Y. J. Hong, Y. C. Kang, *ACS Nano* **2015**, *9*, 4026.
- [46] J. S. Cho, Y. J. Hong, J.-H. Lee, Y. C. Kang, *Nanoscale* **2015**, *7*, 8361.
- [47] W. Wang, M. Dahl, Y. Yin, *Chem. Mater.* **2013**, *25*, 1179.
- [48] Y. Liu, Y. Luo, A. Elzatahry, W. Luo, R. Che, J. Fan, K. Lan, A. Al-Enizi, Z. Sun, B. Lin, Z. Liu, D. Shen, Y. Ling, C. Wang, J. Wang, W. Gao, C. Yao, K. Yuan, H. Peng, Y. Tang, Y. Deng, G. Zheng, G. Zhou, D. Zhao, *ACS Cent. Sci.* **2015**, *1*, 400.
- [49] M. Casas-Cabanas, G. Binotto, D. Larcher, A. Lecup, V. Giordani, J.-M. Tarascon, *Chem. Mater.* **2009**, *21*, 1939.
- [50] L. Lu, L. Li, X. Wang, G. Li, *J. Phys. Chem. B* **2005**, *109*, 17151.
- [51] O. Warschkow, D. E. Ellis, J. Hwang, N. Mansourian-Hadavi, T. O. Mason, *J. Am. Ceram. Soc.* **2002**, *85*, 213.
- [52] G. Binotto, D. Larcher, A. S. Prakash, R. Herrera Urbina, M. S. Hegde, J.-M. Tarascon, *Chem. Mater.* **2007**, *19*, 3032.
- [53] I. Wærnhus, T. Grande, K. Wiik, *Solid State Ionics* **2005**, *176*, 2609.
- [54] B. Kong, J. Tang, Y. Zhang, C. Selomulya, X. Gong, Y. Liu, W. Zhang, J. Yang, W. Wang, X. Sun, Y. Wang, G. Zheng, D. Zhao, *J. Am. Chem. Soc.* **2015**, *137*, 4260.
- [55] Y. Yao, N. Liu, M. T. McDowell, M. Pasta, Y. Cui, *Energy Environ. Sci.* **2012**, *5*, 7927.
- [56] H. Wu, G. Chan, J. W. Choi, I. Ryu, Y. Yao, M. T. McDowell, S. W. Lee, A. Jackson, Y. Yang, L. Hu, Y. Cui, *Nat. Nanotechnol.* **2012**, *7*, 310.
- [57] W.-J. Yu, L. Zhang, P.-X. Hou, F. Li, C. Liu, H.-M. Cheng, *Adv. Energy Mater.* **2016**, DOI: 10.1002/aenm.201501755.
- [58] J. J. Wu, X. J. Lü, L. L. Zhang, Y. J. Xia, F. Q. Huang, F. Xu, *J. Alloys Compd.* **2010**, *496*, 234.
- [59] F. Han, D. Li, W.-C. Li, C. Lei, Q. Sun, A.-H. Lu, *Adv. Funct. Mater.* **2013**, *23*, 1692.